The Molecular Mechanism Underlying Recruitment and Insertion of Lipid-Anchored LC3 Protein into Membranes

ARTICLE *in* BIOPHYSICAL JOURNAL · NOVEMBER 2015

Impact Factor: 3.97 · DOI: 10.1016/j.bpj.2015.09.022

6 AUTHORS, INCLUDING:

Lipi Thukral

Institute of Genomics and Integrative Biology

11 PUBLICATIONS **49** CITATIONS

SEE PROFILE

Divya Murthy

Institute of Genomics and Integrative Biology

2 PUBLICATIONS **5** CITATIONS

SEE PROFILE

Nikhil Agrawal

University of KwaZulu-Natal

1 PUBLICATION **0** CITATIONS

SEE PROFILE

Article

The Molecular Mechanism Underlying Recruitment and Insertion of Lipid-Anchored LC3 Protein into Membranes

Lipi Thukral,[1,*] Durba Sengupta,[2] Amrita Ramkumar,[1] Divya Murthy,[1] Nikhil Agrawal,[1] and Rajesh S. Gokhale[1,*]
[1]CSIR-Institute of Genomics and Integrative Biology (IGIB), New Delhi, India; and [2]CSIR-National Chemical Laboratory (NCL), Pune, India

ABSTRACT Lipid modification of cytoplasmic proteins initiates membrane engagement that triggers diverse cellular processes. Despite the abundance of lipidated proteins in the human proteome, the key determinants underlying membrane recognition and insertion are poorly understood. Here, we define the course of spontaneous membrane insertion of LC3 protein modified with phosphatidylethanolamine using multiple coarse-grain simulations. The partitioning of the lipid anchor chains proceeds through a concerted process, with its two acyl chains inserting one after the other. Concurrently, a conformational rearrangement involving the α-helix III of LC3, especially in the three basic residues Lys^{65}, Arg^{68}, and Arg^{69}, ensures stable insertion of the phosphatidylethanolamine anchor into membranes. Mutational studies validate the crucial role of these residues, and further live-cell imaging analysis shows a substantial reduction in the formation of autophagic vesicles for the mutant proteins. Our study captures the process of water-favored LC3 protein recruitment to the membrane and thus opens, to our knowledge, new avenues to explore the cellular dynamics underlying vesicular trafficking.

INTRODUCTION

The membrane localization of many proteins is dependent on lipid modifications that impart distinct attributes to its functionality (1). Such lipidated proteins can convert between membrane-free and membrane-associated states by attachment of lipids with a particular chemical composition. These lipid attachments, mostly consisting of either myristate, palmitate, farnesyl, or geranylgeranyl moieties, direct proteins to various cell membranes. In recent years, protein lipidation reactions and their structural characterizations have been a major focus of interest (2–6). Although the role of covalent lipid modifications in initiating key signaling is well established, the mechanism of transition from the cytoplasmic protein to the membrane-associated state is poorly understood.

Early reports on the association of Ras protein with membranes gave impetus to this field, providing initial insights into trafficking and signaling of these lipid-modified proteins (7,8). These studies triggered a multitude of experimental and computational studies examining the functioning of Ras proteins and their association with membranes (3–6,9–20). The role of hydrophobic chains in promoting membrane binding, as well as specific membrane targeting, is well established. However, there is a debate as to whether the lipid chain alone is sufficient to provide stable membrane binding (21), or whether a combination of protein-mediated interactions and the acyl chain is required for insertion of the protein into membranes (22–24).

Here, we study a unique covalent modification of the microtubule-associated protein light chain 3 (LC3), a key protein required during initiation of the autophagy process (25). The cytosolic form of LC3 is conjugated reversibly to phosphatidylethanolamine (PE), resulting in lipid-modified LC3 that stably associates with the autophagosome membrane (Fig. 1, *a* and *b*) (26). In many LC3 homologs, including yeast Atg8, the lipid anchor attaches to the protein via a conserved Gly^{120} residue, as shown in Fig. 1 *c*. Two features of LC3 are of particular interest: 1) its role in membrane biogenesis through lipidation (27), and 2) its association with the autophagosome membrane (28). Membrane biogenesis involves de novo the formation of a crescent-shaped double-membrane structure called the isolation membrane (or phagophore) that sequesters the cargo before forming a vesicle (the autophagosome). The final stage requires fusion of the autophagosome with lysosomes and subsequent degradation of the cargo. During the initial stages of phagophore formation, LC3 is known to interact with other autophagic proteins from the endoplasmic reticulum membranes, which aid in the formation of a mature double-membrane autophagosome (29). Additionally, LC3 plays an important role in autophagosome transport through the recruitment of specific motor proteins, which culminates in hemifusion of the autophagosome and lysosome membranes. Given the importance of posttranslationally attached PE in controlling LC3 behavior, dynamic monitoring of the association of lipidated LC3 with the membrane can reveal mechanistic insights into the formation of autophagosome assembly.

Submitted June 15, 2015, and accepted for publication September 18, 2015.
*Correspondence: rsg@igib.in or lipi.thukral@igib.in
Lipi Thukral and Durba Sengupta contributed equally to this work.
Editor: Markus Deserno.

0006-3495/15/11/2067/12
http://dx.doi.org/10.1016/j.bpj.2015.09.022

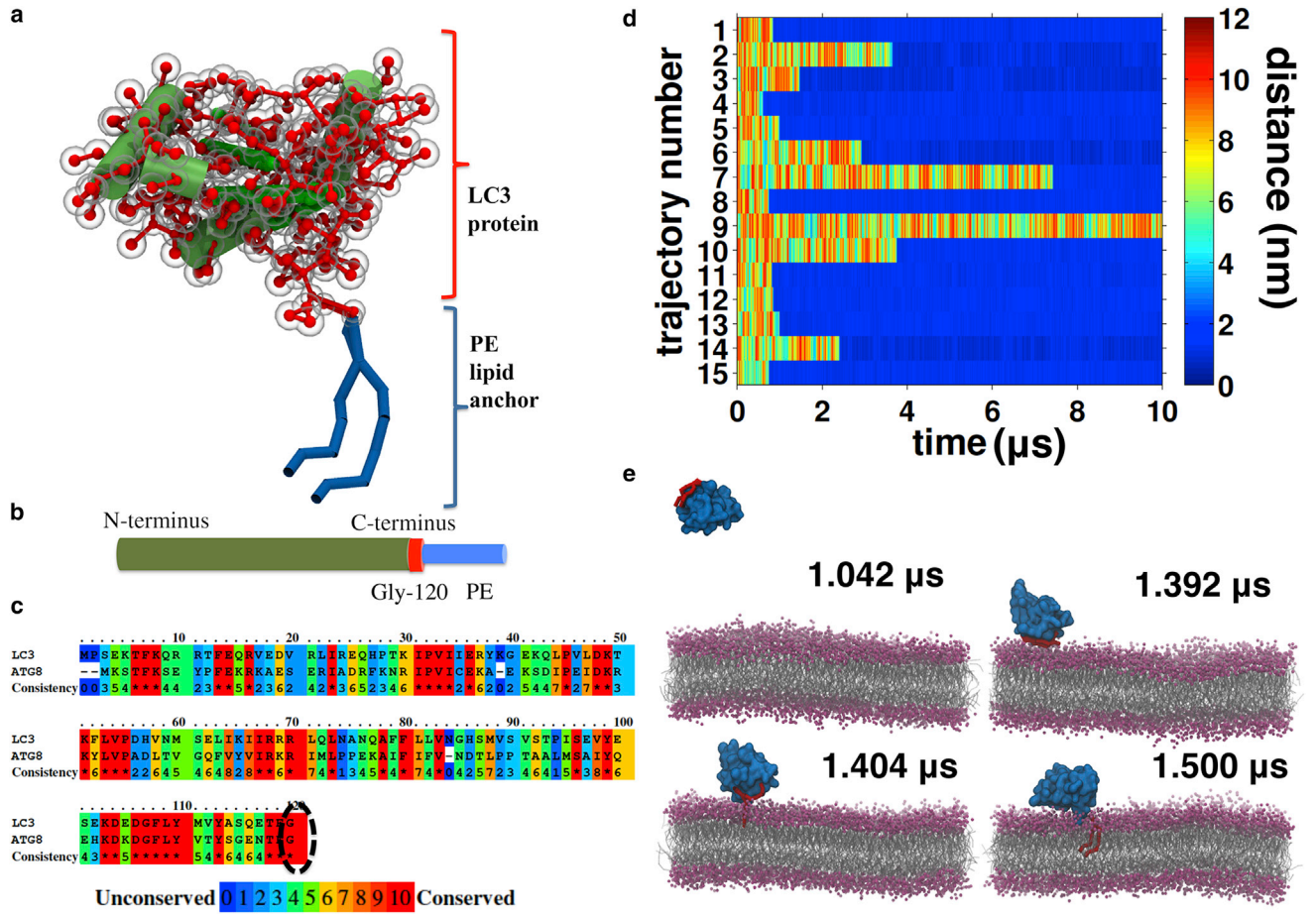

FIGURE 1 Structural properties of LC3-PE and its spontaneous membrane insertion. (*a*) The structure of the LC3 protein shown in CG representation, with the PE chain covalently attached to its C-terminus. The secondary structural elements are comprised of four α-helices and five β-sheets shown in green. (*b*) A schematic representation of the LC3-PE protein linked with the lipid anchor chain (*blue*) and Gly^{120} at the C-terminus (*red*) highlighted for clarity. (*c*) Amino acid alignment of LC3 with its homolog yeast protein Atg8, showing the conserved Gly^{120} residue. (*d*) Time evolution of the distance between the PE chain of LC3 and the POPC bilayer along the 15 trajectories. The protein inserts in trajectories 1–8 and 10–15. In trajectory 9, the PE chain insertion is not observed. (*e*) Snapshots of LC3-PE insertion. The structures were extracted from trajectory 3, one of the representative productive trajectories. The LC3-PE transition from an aqueous state (water not shown for clarity) to the membrane-bound and finally to the membrane-inserted state is shown. To see this figure in color, go online.

We report here the partitioning of the lipid anchor of LC3 into the bilayer, with the starting structure placed in the aqueous phase. We performed multiple independent molecular dynamics (MD) trajectories, with a combined simulation time of 600 μs, which corresponds to 2.4 ms of effective time. We used the MARTINI coarse-grain (CG) model, which has been applied with remarkable success in the study of lipid domains and protein-lipid interactions (30–33). Spontaneous insertion events of the lipid anchor were observed in >10 simulations, reproducing the observed membrane-inserted state of LC3-PE (26,34).

Subsequently, we decipher the molecular mechanism of protein insertion into the bilayer with high statistical reliability. Combining computational predictions and experimental analysis of live-cell imaging, we were able to characterize crucial residues underlying membrane recognition of the lipidated LC3 protein. Further, we discuss the implications of perturbations introduced within the protein (through mutations) and the membrane (by introducing negatively charged lipids), which allowed us to study the relative contributions from fundamental hydrophobic and electrostatic interactions.

MATERIALS AND METHODS

We performed 15 simulations of lipidated protein interacting with 1-palmitoyl-2-oleoyl-*sn*-glycero-3-phosphocholine (POPC) bilayers. In addition, we simulated the lipidated LC3 protein with a heterogeneous bilayer. To comprehensively explore the LC3-protein-membrane dynamics, we investigated the effect of mutations in the LC3 protein and performed control simulations where the LC3 protein was not lipidated. The details of preparation of the starting structures, the bilayer compositions, and the MD protocol are provided below. A comprehensive list of simulations is given in Table S1 in the Supporting Material.

Starting structure

The LC3 protein structure was taken from the Protein Data Bank database (PDB: 1UGM (25)). The three missing residues (Thr^{118}, Phe^{119}, and Gly^{120}) in the crystal structure at the C-terminus constituting the hypervariable region were modeled as a random coil, whereas the missing residues at the N-terminus (1–4) were not included. The atomistic structure was equilibrated in water and mapped onto a CG model based on the MARTINI force field (35,36) using the martinize script (37). The standard MARTINI CG parameters (version 2.2) were used to describe the protein, together with an elastic network to define the tertiary structure (35,36). A standard implementation of the elastic network was used with a force constant of 500 kJ/mol. The distance constraints of all secondary structural elements were set to be constant, including the terminal residues.

The PE lipid anchor was attached to the C-terminal glycine residue (Gly^{120}) and the parameters were derived from already existing 1-palmitoyl-2-oleoly-*sn*-phosphoethanolamine (POPE) lipid parameters of the MARTINI force field. Extra bonds were added between the terminal protein residues and the headgroup of the lipid anchor, but not between the lipid tail and the protein to allow full flexibility of the lipid anchor. Two mutant proteins were generated by mutating all the charged residues of α-helix III, i.e., Lys^{65}, Arg^{68}, Arg^{69}, and Arg^{70}, to either all Ala residues in one mutant or all Ile residues in the other. The parameters for the Ala mutant were generated using the martinize script (37). The Ile mutant was generated by replacing the Arg or Lys side chain with Ile. Dummy atoms were attached to the Ile side chain to keep the total number of side-chain beads constant.

Lipid bilayers

The zwitterionic 1-palmitoyl-2-oleoly-*sn*-phosphocholine (POPC) membrane was built by self-assembly of 284 randomly placed lipid molecules. The self-assembled bilayer, consisting of a total of 1136 POPC molecules, was then replicated in the x and y directions and equilibrated for 10 ns. The negatively charged heterogeneous membrane was generated by self-assembly CG MD simulations. In these simulations, POPC, POPE, and cardiolipin (CL) were randomly placed in a simulation box (without protein). Recently, it was reported that LC3 contains CL binding sites and associates with the mitochondrial membrane (38). Thus, the ratios of lipids in the heterogeneous membrane patch were chosen to represent a mitochondrial membrane patch (39). In total, the bilayer contained 568 POPC, 284 POPE, and 284 CL lipids to maintain a ratio of 2:1:1. Subsequently, a production run was performed for 200 ns. After $\approx$100 ns of the simulation, the bilayer was formed with equal distribution of lipids in the two leaflets.

System set-up

In each of the simulations, the protein was initially placed in the aqueous phase, at a distance of $\approx$8 nm from the bilayer center. Each simulation box contained a single lipidated LC3 protein and 1136 lipid molecules in both the charged and uncharged membranes. To allow free diffusion of the LC3 protein in the aqueous layer, the distance between the periodic images of the membrane was chosen to be ~15 nm in height, leading to a final box size of $\approx 18 \times 20 \times 20$ nm and $21 \times 20 \times 20$ nm for the POPC and charged membranes, respectively. In the POPC membrane, 52,290 water beads and two negative counterions (Cl^-) were added by replacing two water molecules so as to produce a neutral system, totalling to 67,346 atoms. In the charged membrane, 57,455 water beads and 282 positive counterions (Na^+) were added by replacing the solvent molecules, totalling to 76,199 atoms. Additional simulations of two mutant proteins, nonlipidated LC3 molecules with membranes, with a pure POPC bilayer were also performed.

MD simulations

The MD simulations were performed using the program GROMACS, version 4.5.5 (40). The MARTINI force field, version 2.2, was used to describe the protein, lipids, and water (35,36). Simulations were performed at 310 K using the Berendsen thermostat (41) with a coupling time of 0.1 ps. The pressure was also coupled (coupling time 1.0 ps, compressibility 5×10^{-5} bar^{-1}) using a semiisotropic coupling scheme where the lateral and perpendicular pressures are coupled independently to maintain a constant pressure of 1 bar (41). The nonbonded interactions were treated with a switch function from 0.0 to 1.2 nm for the Coulomb interactions and 0.9 to 1.2 for the LJ interactions (pair-list update frequency of once per 10 steps). Periodic boundary conditions were used and the time step used to integrate Newton's equations of motion was 20 fs.

Analysis of trajectories

The trajectories were analyzed using a number of order parameters that capture principal aspects of protein and membrane dynamics.

Membrane thickness and density

These parameters were calculated using analysis tools developed previously (42). The translational motion of the protein was removed (i.e., the position of the center of mass of the protein was constant) before calculating the distance-dependent membrane-thickness profile. The thickness was calculated as the average distance between two phosphate beads (PO4) in the headgroup of POPC. To calculate the thickness, different timepoints during the course of the simulations were determined and the values of thickness from the given time point to 100 ns were averaged.

Pressure profiles

The pressure tensor was calculated over the entire system by dividing it into grids of 0.1 nm. For a system with planar symmetry, such as a lipid bilayer, the local pressure can be divided into planar, $P_L = (P_{xx} + P_{yy})/2$, and normal (along the membrane normal direction), $P_N = P_{zz}$, components. The lateral pressure profile, $p(z)$ is then defined as a difference between the lateral and the normal components of the pressure tensor, that is, $p(z) = P_L - P_N$. The lateral pressure profiles were calculated as described in previous work (43,44) after removal of the center-of-mass motion of the protein.

Spontaneous curvature

The spontaneous monolayer curvature, c_0, was calculated from the first moment of the stress (44):

$$c_0 = \frac{1}{k_m} \int_0^d z\, p(z)\, dz, \tag{1}$$

where, k_m is the monolayer bending modulus, equal to half the bilayer bending modulus ($k_b/2$), z is the distance across the membrane relative to the center of the bilayer ($z = 0$), and d is the thickness of the monolayer. Since the expression is not independent of the choice of definition of local pressure, it should be used as a qualitative measure. Positive values for the radius of spontaneous curvature reflect an increased preference for positively curved surfaces (such as in micelles and pores), and increasingly negative values correspond to an increasing preference for negatively curved surfaces (such as in stalks and inverted hexagonal phase) (44).

The standard error of the mean quantifies the precision of the mean

It is a measure of how far the sample mean is likely to be from the true population mean. It takes into account both the standard deviation and the sample size. Error bars were also calculated for the residue-wise

distribution histogram and the lateral pressure profiles. The statistical error on the above parameters was estimated through the standard error of its mean as follows:

$$\sigma = \left(\frac{\sum_{i=1}^{n} (a_i - \overline{a})^2}{(n-1)n} \right)^{1/2} \quad (2)$$

$$\overline{a} = \frac{\sum_{i=1}^{n} a_i}{n}, \quad (3)$$

where a_i is the generic parameter evaluated in the ith subset. Here, n corresponds to 14 independent trajectories.

Other parameters

The probability of contact formation was calculated by defining a contact when the distance between each protein residue in α-helix III and the membrane is $<$0.8 nm. Protein localization with respect to the membrane (see Fig. 5) is categorized into three phases depending on the distance of the protein from the center of mass of the bilayer: the water-associated (WA) phase, at $\geq$6 nm, the membrane-associated (MA) phase, at $\geq$3 and $\leq$6 nm, and the membrane-inserted (MI) phase, at $\leq$3 nm.

Experimental protocol

Plasmids and antibodies

LC3B mutants were cloned in pmCherry-C1 vector (Clonetech, Mountain View, CA). The mutants for LC3 were generated using two-step-overlap polymerase chain reaction with flanking end primers. Primers for cloning and mutation are listed in Table S2. Anti-mCherry antibody was purchased from Abcam (ab167453, Cambridge, United Kingdom). For immunoblot analysis, cells were lysed and analyzed by SDS/PAGE and Western blot according to standard protocols. β-actin (ab20272) was used as a normalizing control.

Cell culture, transfections, and Western blot

Hela and HEK cells were grown in Dulbecco's modified Eagle's medium supplemented with 10% fetal bovine serum (heat inactivated) at 60–80% confluence at 5% CO_2 levels. Cells were transfected to 60% confluency using Lipofectamine 2000 (11668019, Invitrogen,:Carlsbad, CA) for expression of plasmid according to the manufacturer's instructions. Transfected cells were analyzed 48 h after transfection. For live imaging, cells were grown in two-chambered Nunc chamber slides (Lab Tek chambered coverglass, 155380, Thermo Fisher Scientific, Waltham, MA).

Confocal microscopy and data processing of mCherry-LC3 puncta

Cells transiently expressing the indicated mCherry fusion proteins were treated under normal conditions. Fluorescent live samples were visualized on a Zeiss LSM 710 confocal system (built around a Zeiss Axiovert 200 M inverted microscope), using a 63×, 1.3 NA oil objective. Data were collected as z-stacks with approximately 25 planes and 0.5–0.6 μM spacing between each plane. The merged image was created using the maximum-intensity projection software built into the Zeiss system. The formation of punctate structures was estimated using Volocity software. The average number of puncta per cell was calculated and plotted using GraphPad.

All data were analyzed with Prism software (GraphPad, San Diego, CA) using the two-tailed unpaired Student t-test. All values are expressed as the mean $\pm$ SD. Error bars represent the standard deviation. Each experiment was replicated at least three times as independent biological replicates, as indicated in the figure legends. Differences were considered significant at $^{*}p \leq 0.05$, $^{**}p \leq 0.01$, and $^{***}p \leq 0.001$, respectively.

RESULTS

Insertion of the covalently attached PE chain of LC3 into the membrane

To explore the unbiased insertion of the protein into the bilayer, we performed 15 independent simulations with the starting structure of LC3-PE placed $\approx$8 nm from the bilayer center composed of zwitterionic POPC lipids. In our simulations, no apriori contacts or restraints were applied between the protein and the membrane. The time evolution of the conformational transitions of lipid chain bound to LC3 is displayed in Fig. 1 *d* using the distance between the PE and the membrane as an order parameter. Spontaneous insertion of the hydrophobic anchor of protein into the membrane (dark blue, $d \approx 0.5$ nm) is observed in 14 of 15 trajectories (1–8,10–15). In these 14 productive cases, once the PE inserts into the hydrophobic core, the interaction with the lipid bilayer is highly stable. Most of the trajectories lead to insertion within 4 μs in the simulations. However, in the single nonproductive ninth trajectory, insertion of the PE is not observed.

Fig. 1 *e* demonstrates the progress of LC3-PE insertion during one of the representative trajectories. The starting structure was placed in the aqueous phase (Fig. 1 *e*, *upper left*) and the diffusion of LC3 toward the membrane was observed (Fig. 1 *e*, *upper right* to *lower right*). All simulations where insertion has been achieved follow a similar course of molecular interactions. The initial event of protein recruitment to the lipid involves docking to the surface of the membrane, which is crowded with polar headgroups. After the protein is completely bound, a sequential stepwise insertion of the acyl chains commences in a concerted process, with the two acyl chains inserting one after the other (Fig. 1 *e*, *lower right*). Finally, the lipid anchor of the protein is completely buried in the membrane along with the acyl chain of POPC lipids. Previous computational studies with other lipidated proteins employed preformed protein-membrane contacts, and the simulations were performed using an atomistic force field (11,12). However, unbiased docking of protein onto the lipid membrane using atomistic simulations is difficult due to currently accessible timescales. Our approach, using CG simulations of the full-length protein placed far from the bilayer successfully permits us to trace the MI state of the lipidated LC3 protein, as expected to proceed experimentally (26,34).

The membrane targeting mechanism of lipidated LC3

Deciphering the membrane contact sites of LC3

A critical question that arises is, how does the protein achieve the MI state? Since lipid modification of proteins increases their affinity for membranes, the partitioning of lipid chains into the membrane is deterministic to the function of

the protein. Fig. 2 *a* plots the distance of each amino acid residue from the center of mass of the bilayer. This illustrates the interaction of the LC3 polypeptide chain with the membrane after insertion of the PE chain. Residues in the segment from α-III, β-IV, and β-V exhibit close contact with the membrane in all simulations (see error bars). Structurally, this region corresponds to a rather large contact interface, containing several basic residues, as highlighted in blue in Fig. 2 *b*. Before insertion, it appears that the process of protein interaction with the membrane is primarily driven by a random diffusion process, since all the regions of the protein show an equal propensity to approach the membrane interface (see Fig. S1).

Further, to determine the protein regions driving the insertion process, we calculated the time evolution of secondary structural elements of the LC3. Fig. 2 *c* shows that the α-III contacts the membrane before β-IV, and β-V in one of the representative productive trajectories. Since LC3 is doubly lipidated in the form of PE, we also monitored the time occurrence of each acyl chain insertion and found that in 9 of 14 productive simulations, the two acyl chains insert one after another (Fig. S2).

Further, as a measure of validation, the probability of contact formation of each residue in α-III with the membrane was measured for all 14 productive simulations and compared to a single nonproductive simulation (Fig. 2 *d*). The productive trajectories revealed that most of the residues in α-III form a strong association with the membrane (contact probability $\approx$0.5). Interestingly, in the single nonproductive simulation, these residues form few contacts with the membrane (contact probability $\leq$0.006). Most of the residues populating this cluster are basic in nature, including Arg^{68}. Arginine-rich patches are often the most common scaffold of the cell-penetrating peptides that efficiently enter into cells (45). In a recent study, it was suggested that Arg^{68} plays an essential role in the autophagic activity of LC3 (46).

Taken together, these data suggest a possible mechanism for LC3 insertion into membranes. The dynamic changes in the lipidated LC3 protein are induced by specific protein-lipid interactions. A cluster of basic amino acids in the α-helix III region determines and facilitates the insertion of the PE anchor by electrostatically driven protein-membrane association. This occurs in all productive trajectories but is absent in the one nonproductive simulation. Similar findings have been reported previously for myristoylated C-kinase substrate, where a cluster of basic residues is essential for membrane insertion with the myristoyl chain (23).

In silico mutation of a cationic patch weakens membrane interactions

Our data suggest a model where the positively charged patch in α-helix III of LC3 directly binds to the membrane, thereby assisting in the LC3-PE insertion process, as shown in the pre- and postinsertion stages in Fig. 3 *a*. To test this hypothesis, all basic residues of α-helix III, i.e., Lys^{65}, Arg^{68}, Arg^{69}, and Arg^{70}, were replaced with Ala and Ile residues in the two corresponding mutants. Trajectories of these Ala and Ile mutants were run on timescales similar

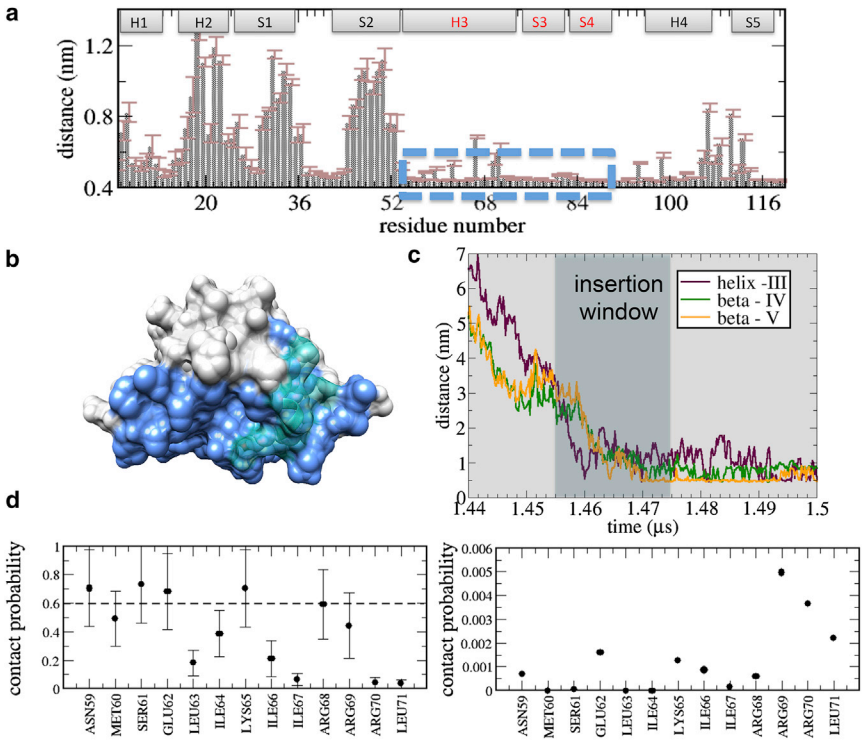

FIGURE 2 Localization of protein onto the membrane. (*a*) The residue-wise distribution of the distance of the protein from the membrane. The secondary structural elements are mentioned at the top. The highlighted box shows the structural interface that makes close contact with the membrane in all simulations. Error bars show the standard error calculated for the period of the trajectory subsequent to insertion, for all simulations combined. In addition, see Fig. S1 for the pre-insertion-phase residue-wise distribution. (*b*) LC3 displays a remarkably asymmetric surface charge distribution with a contiguous segment of positively charged surface (*dark blue*) and the α-helix III region highlighted in light blue. (*c*) Time evolution of the distance of α-helix III, β-sheet IV, and β-sheet V from the membrane in one of the representative productive simulations. For details of the time kinetics of individual acyl chain insertion events, see Fig. S2. (*d*) The probability of contact formation of α-helix III residues with the membrane. Data on the left are calculated from all productive LC3-PE simulations of LC3 after insertion and those on the right from the single nonproductive trajectory 9. The error bars shown represent the mean $\pm$ SE of all simulations. A distance cutoff of 0.8 nm between each protein residue and the membrane was used. To see this figure in color, go online.

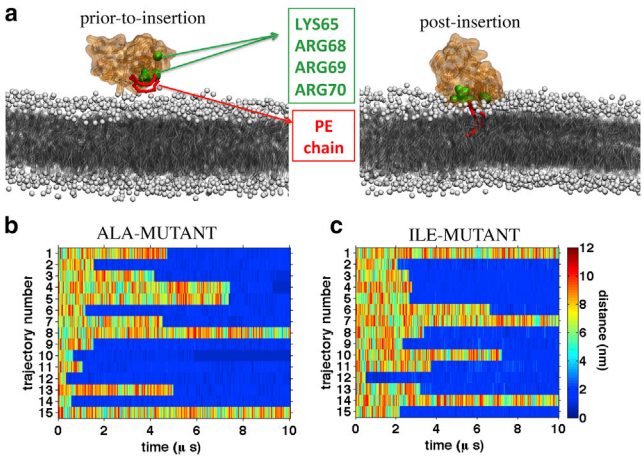

FIGURE 3 In silico mutations reveal altered protein-membrane interactions. (*a*) Snapshots displaying the mutated residues at the pre- and postinsertion states of the LC3 protein. (*b* and *c*) The time course of the *Z*-component of the center of mass of the membrane and the PE chain of Ala- and Ile-mutant proteins, respectively The distance color bar is shown on the right, with the dark blue color indicating membrane insertion of the lipid anchor. To see this figure in color, go online.

to that for the wild-type LC3 protein, i.e., 15 simulations of 15 μs each for the two mutants. As shown in Fig. 3 *b*, the insertion properties of the mutant proteins can be examined by monitoring the distance of the lipid anchor to the membrane. Both the mutants show a decrease in the membrane-interface population, with the Ile mutant having three nonproductive trajectories compared to a single nonproductive simulation in the wild-type protein (see Fig. 1 *d*). The Ala-mutant protein shows a slight variation, with an average insertion time (τ) of 1.35 μs compared to 3.31 μs for the Ile-mutant protein. It is worth noting, however, that the timescale mentioned here should be considered as a qualitative description of association due to the nature of the CG force field. In comparison to atomistic models, CG models are faster, and the simulation times reported here are actual simulation times, which, multiplied by a factor of 4, gives the effective times (35,36).

It is encouraging that the relatively small difference in charges in α-helix III has resulted in a modified behavior of the MA state of LC3. Interestingly, in a recent study, Arg^{68} was also found to be an essential residue, and its mutation leads to weakened C-terminal cleavage efficiency (46). In addition, these results also suggest that the method is capable of correctly reporting the effects of residue mutations on protein-membrane interactions.

Experimental validation of key residues facilitating membrane targeting

LC3 is a classical autophagic protein that is known to associate with vesicular membranes, thereby marking them for degradation. During the autophagy process, membrane recruitment of LC3 at the isolation-membrane structure results in the formation of a vesicle, the autophagosome. Thus, to further evaluate the biological role of these structural patterns, we monitored the ability of mutant proteins to form autophagosomes by a live-cell imaging technique. We generated a series of LC3 mutants tagged with mCherry, namely, K65A-R68A, K65A-R68A-R69A, K65A-R68A-R69I, and K65A-R68A-R69E, and explored ex vivo its role in autophagosome formation.

The LC3B mutants were transiently expressed in the human embryonic kidney (HEK) mammalian cell line. Fig. 4 *a* shows confocal images of HEK cells expressing the wild-type and mutants of LC3B. We assessed the steady-state levels of autophagosomes by enumerating the mCherry-LC3B puncta (Fig. 4 *b*) and further monitored the amount of LC3B-PE formed in these cells. The formation of LC3 puncta is a direct measure of the number of autophagosomes formed within a cell. Remarkably, the K65A-R68A-R69E mutant showed a significant reduction in the number of LC3B puncta, whereas the number of autophagosomes formed in cells expressing K65A-R68A-R69A and K65A-R68A-R69I was moderately lower than in the wild-type protein. These results suggest that R69 is critical during the formation of autophagosomes and that mutating it to a negatively charged residue (R69E) severely affects the autophagosome formation. To check whether the mutant proteins are not affecting LC3-PE conjugation, we also monitored posttranslational modification of LC3B for the mutants by Western blot, as shown in Fig. 4 *c*. Immunoblot analysis of the LC3B mutants using the mCherry antibody revealed no differences in the levels of LC3B-PE expression.

A negatively charged membrane alters the residence time of protein before insertion

Several factors govern peripheral protein-membrane association, and many can be understood in terms of electrostatic and hydrophobic effects. To gain further insight, we decided to probe this interplay by modifying the bilayer composition by including negatively charged lipids. Our focus will be, in particular, on illustrating how environmental variations can be used to rationalize the origin of the driving forces that reflects the mechanism of lipidated protein insertion. We varied the membrane lipid composition from zwitterionic POPC to a more complex physiological membrane composed of POPE, POPC, and CL in a 2:1:1 ratio (see Materials and Methods for details). The distinctive feature of this heterogeneous membrane is the shape and charge of CL, which consists of four acyl chains and the large negative charge of the phosphatidyl headgroups. Fig. 5 *A* shows that the lipidated protein inserts completely into the negatively charged lipids in all 15 independent simulations, with an average insertion time (τ) of 1.25 μs compared to 2.57 μs in POPC bilayer.

Fig. 5 *B* reveals the time evolution of the location of protein categorized specifically into the WA (protein-membrane distance $\geq$6 nm), MA (protein-membrane

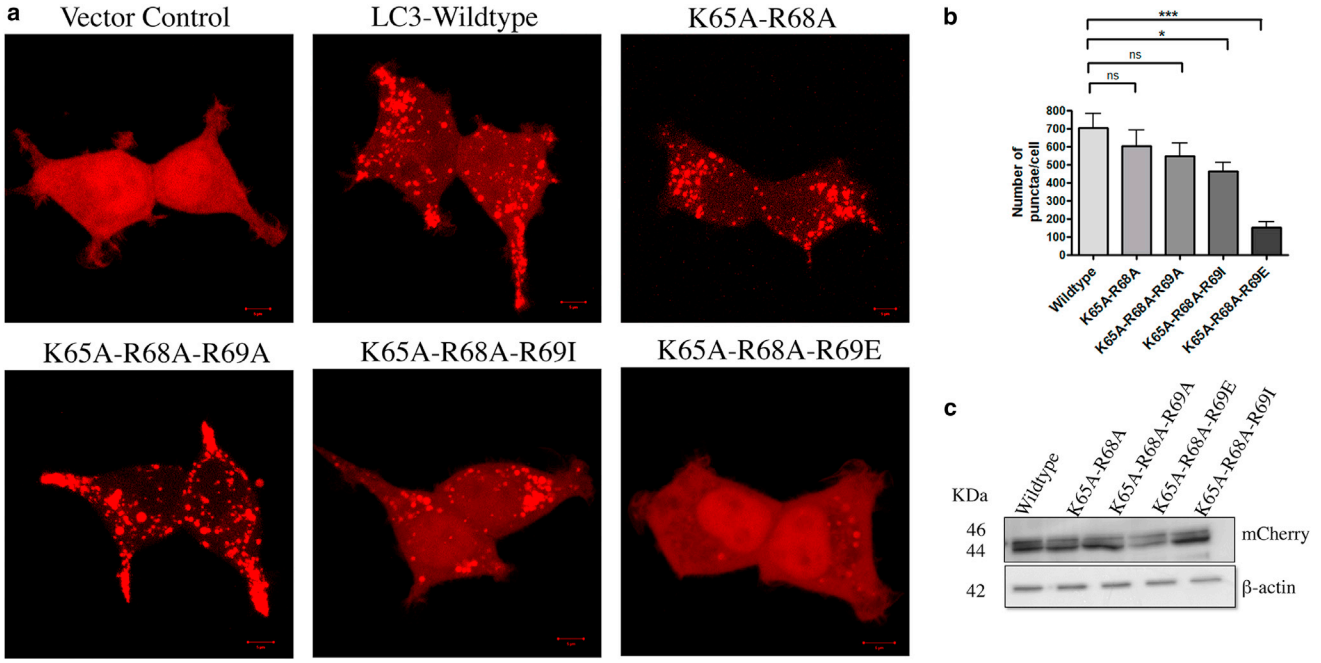

FIGURE 4 Experimental validation of how mutation of residues crucial to membrane targeting affects autophagosome formation. (*a*) Immunofluorescence micrographs of HEK cells cotransfected with mCherry-LC3 mutants along with wild-type LC3 and a vector control. The formation of punctate structures was notably reduced in the LC3-K65A-R68A-R69E mutant. Scale bars, 5μm. (*b*) Quantitation of the number of puncta in cells transfected with wild-type LC3 and mutants using Volocity software ($n \geq 10$ from three independent experiments). Bars represent the mean $\pm$ SD across replicates. *$p \leq 0.05$; **$p \leq 0.01$; and ***$p \leq 0.001$. (*c*) Western blot analysis for monitoring LC3 flux. HEK cell lysates expressing mCherry-LC3 and LC3 mutants were subjected to immunoblotting with anti-mCherry and anti-β-actin antibodies. The presence of both nonlipidated and lipidated LC3 was observed. To see this figure in color, go online.

distance $\geq$3 nm and $\leq$6 nm), and MI (protein-membrane distance $\leq$3 nm) states of four representative trajectories (trajectories 3, 4, 14, and 15). The colored bars in the figure indicate the different states (maroon, yellow, and dark blue for the WA, MA, and MI states, respectively). The existence of these states in all 15 trajectories is shown in Fig. S3. We found that, contrary to what would be expected, the protein is able to form stable binding at the water-membrane interface ($Z \approx 5$ nm (Fig. S3, *yellow*)) before insertion in most of the simulations. Also, the molecular signature of the protein on the membrane is indeed associated with residues involved in the α-helix III region (data not shown). Together, these results suggest that protein-membrane docking is governed by electrostatic interactions, whereby anionic lipids orient and steer the protein toward the membrane surface, followed by the final stage of the MI state, which is driven by hydrophobic forces of acyl chains.

Control simulations of the nonlipidated LC3 protein

The lipidated protein clearly inserts into a zwitterionic bilayer in 14 of 15 trajectories (Fig. 1 *d*) and into a negatively charged bilayer in all trajectories (Fig. 5 *A*). Further, to analyze the contributions of the hydrophobic lipid anchor of the protein, control simulations of nonlipidated protein in the membrane environment were performed (see Materials and Methods). First, the nonlipidated protein favors the aqueous water phase, with the protein distance ranging from 4.5 nm to 8.5 nm from the center of the bilayer, as shown in Fig. 6. Second, the protein undergoes fast-time-scale membrane association-dissociation events. Clearly, the hydrophobic anchor attached to the protein contributes actively in the insertion process of the protein. Since the nonlipidated protein was designed as a control to mimic the in vivo cytosolic LC3 protein, these results further strengthen our hypothesis that interplay between the lipid anchor and the cluster of basic residues is crucial for protein insertion.

Bilayer perturbations

The membrane-perturbing propensity of LC3 protein was determined by measuring the density and thickness of the bilayer (Fig. S4). At the point of PE insertion, localized changes in the density of the acyl chains and the membrane thickness are observed, as shown in Fig. S4, *A* and *B*, respectively. However, during the course of the simulations, the membrane perturbations equilibrate (Fig. S4, *C* and *D*). Further, a comparison with the control simulation of the pure POPC bilayer reveals only marginal differences in

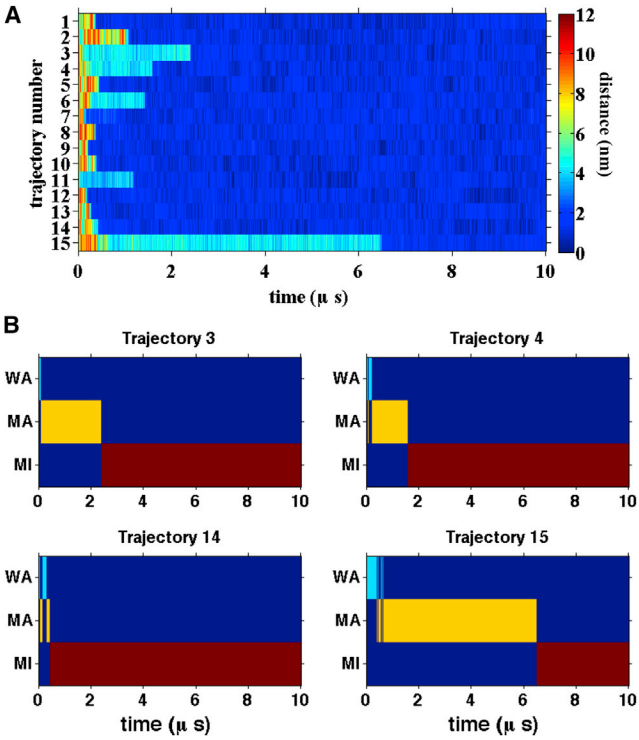

FIGURE 5 Role of electrostatistics in protein-membrane interaction. (*A*) Time evolution of the distance between the PE chain of the LC3 and the negatively charged bilayer along the 15 trajectories. The lipid anchor of the protein inserts in all trajectories. (*B*) Localization of the protein during four representative trajectories. The bars represent the existence of WA (*maroon*), MA (*yellow*), and MI (*dark blue*) states. See Materials and Methods for details regarding the definition of the different parameters. To see this figure in color, go online.

the bilayer properties (Fig. S4, *E* and *F*). Although a single LC3 is not able to induce large perturbations, we believe that the effect of LC3 on the reorganization of membrane may be additive and that at higher protein/lipid ratios, the variations measured above could be higher.

Fig. 7 depicts the lateral-pressure profiles of the LC3-anchored membrane and the pure bilayer in black and red, respectively. The pressure profiles were calculated after insertion of the POPC chain and are averaged over the membrane lateral area and all productive trajectories, based on a previous implementation (43) (see Materials and Methods for details). After the insertion of LC3-PE, the lateral pressure near the lipid tails is decreased by 100 bar. However, the variations near the center of the bilayer were minimal. Counterintuitively, the pressure profiles appeared to be symmetric at both bilayer leaflets despite the insertion of the POPC chain. To test the effect of the lipid chain, we calculated the pressure profile within 1 nm of the protein (see Fig. S5) for a few representative simulations. Comparison of the two leaflets clearly shows the deviations between them. It thus appears that the large bilayer used in our simulations appears to equilibrate the effect of the lipid chain over the entire bilayer. Proteins docking with lipid surfaces can induce changes in the local spontaneous curvature, causing deviations from the lamellar phase (47).

The pressure profiles of membranes can be correlated with elastic properties such as local spontaneous curvature, which is calculated from the first moment of the pressure profile (48); for an extended discussion, see (49). The pressure profile calculated over the entire bilayer was used to calculate the monolayer spontaneous curvature. Since the membrane tension is calculated to be zero, the bilayer midplane was used as the Gibbs dividing surface of the monolayer. Within these assumptions, the LC3-bound membrane was calculated to have a spontaneous curvature close to 0.0 nm^{-1}, in comparison with the pure POPC bilayer, which has a curvature of -0.15 nm^{-1} (31). We thus see an increase in the local spontaneous curvature upon LC3 insertion. In general, negative values for the radius of

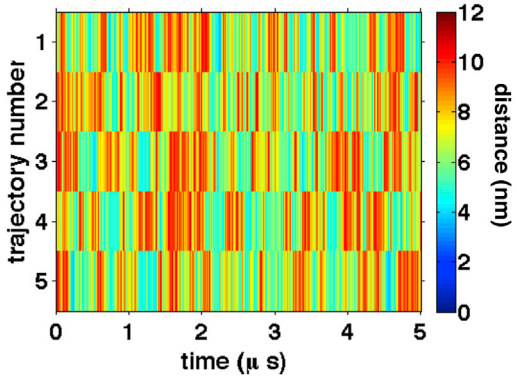

FIGURE 6 The nonlipidated protein. Shown is a time series of the distance between the nonlipidated LC3 protein and the center of mass of the membrane across five independent simulations. The protein tends to be in the aqueous phase (distance $\geq$ 6 nm), with fast-timescale membrane dissociation events. The color gradient reflects the distance (in nanometers) for the MA (*green*) and WA (*orange/red*) states. To see this figure in color, go online.

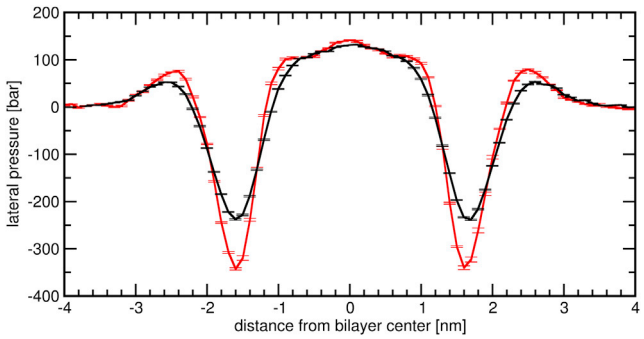

FIGURE 7 Pressure profiles. Comparison of the lateral pressure profiles of the productive simulations (*black*) and the pure POPC bilayer without protein (*red*) as control simulations. The pressure profiles were calculated after the insertion of the lipid anchor for the productive simulations. The error bars shown represent the standard error between the simulations. For further details, see Materials and Methods. To see this figure in color, go online.

spontaneous curvature are indicative of a preference for concave-shaped curved surfaces (inverted phases, stalks) and positive values indicate a propensity toward convex-shaped curved surfaces (such as in vesicle budding) (50). The increase in spontaneous curvature of the bilayer arises from the decrease in negative pressure arising from the acyl chain region of the bilayer, as seen in Fig. 7. The values reported should be considered to be qualitative, since discrepancies have been observed with calculation of the lipid spontaneous curvature, and especially the Gaussian curvature modulus, from this method and others (51). During autophagy, membrane recruitment of LC3 at the isolation membrane results in the formation of a vesicle, the autophagosome. The finding on spontaneous curvature calculated from our simulations suggests a possible initiating role of LC3 in stabilizing highly curved organelles like autophagosomes.

DISCUSSION

Several problems have impeded our understanding of lipid-modified proteins and their interaction with phospholipid bilayers, in particular, the difficulty in obtaining protein crystals with the lipid anchor (52). Computer simulations have now started to reveal the molecular details of their conformational dynamics and provided putative contributions of both protein and membrane lipids (11–13,16,20,53,54). Among the earliest reports, atomistic MD simulations of membrane-bound H-ras protein predicted two modes of membrane binding. In GTP-bound conformations, the α4 helix of the G domain facilitates membrane association, whereas GDP-bound structures favored electrostatic interactions between basic residues of the C-terminal region and the membrane (12). In all previous reports, simulations begin from a well-defined membrane-bound conformer, and therefore, details of key transition events such as membrane binding are not known. In this work, we have demonstrated spontaneous insertion of aqueous-phase lipidated LC3 into the membrane using unbiased multiple independent microsecond-long simulations performed at physiological temperature. Examination of the events before, during, and after insertion of PE reveals a stagewise process involving contributions from both the lipid anchor and the protein.

Due to the complex nature of lipid anchor insertion, we observe highly stable conformations of the LC3-PE MI phase. This overstabilization of interactions increases the roughness of the energy landscape and hence hinders the rapid sampling of reversible transitions. This is likely why it is extremely difficult to obtain spontaneous reversible transitions of complex processes, even though reasonable agreement between simulations and experiments regarding thermodynamics has been demonstrated for a range of proteins (16,55). In this work, we only used symmetric bilayers, and therefore, protein binding to both the leaflets evolves in a similar manner. Biological membranes contain a heterogeneous mixture of phospholipids, and thus, they can act as guiding forces for molecular recognition. To investigate this phenomenon, we performed multiple LC3 simulations with a lipid bilayer consisting of POPC, POPE, and CL in a 2:1:1 ratio. Permeation of the lipid anchor occurs in all simulations, and interestingly, the insertion time, τ, is greatly reduced. The presence of negatively charged CL significantly alters the kinetics of the first step involving protein-membrane docking. However, the second step of insertion, driven by the hydrophobic anchor, occurs on a slow timescale, as the protein residence time on the membrane is increased.

Consequently, the reactions must be guided by a recognition process, where specific residues determine specificity. Based on several spontaneous insertion events using computer simulations, we were able to identify key residues facilitating the LC3 membrane-targeting process. Our hypothesis was substantiated by a combined in silico and in vitro approach whereby we mutated the basic residue patch consisting of Lys^{65}, Arg^{68}, and Arg^{69} in the α-helix III region. The lipidated form of LC3 stably inserts itself into autophagosome membranes, where it is crucial during phagophore elongation and cargo recognition. Using live-cell imaging, we monitored the presence of the autophagosome and observed a significant decrease in puncta formation in one particular mutant, i.e., K65A-R68A-R69E (Fig. 4). The specific mutant is based on a complete-charge-reversal strategy and severely hampers membrane targeting by the LC3 protein. These data are in concordance with several previous experimental and computational approaches where positively charged residues close to the binding site are responsible for the protein penetration into the membrane (56). Owing to the underlying complexity of such interactions, side-chain orientations of these residues (K65-R68-R69), might also play a major role in membrane association. However, the CG simulations performed in this work provide the determining factors for the progression of a lipidated protein membrane insertion. Future work involving large-scale atomistic simulations might clarify the range in which such side-chain orientations are crucial for guiding the final insertion stage of the lipid anchor.

As with this work, it is also imperative to discuss the possible limitations of the CG MARTINI model, and the conclusions should be carefully interpreted. First, the secondary structure of the protein is restrained during the entire simulation, and therefore, the conformational changes within the protein induced by PE cannot be determined. Second, it is unclear how the water model influences the protein-membrane interactions as the accuracy of electrostatic screening by the water model is not adequate (37).

Although LC3 may have many cellular functions, it is best characterized as the master regulator of autophagy, a process by which the cell forms a specialized vesicle, the autophagosome, to degrade the cellular waste. It is a multistep

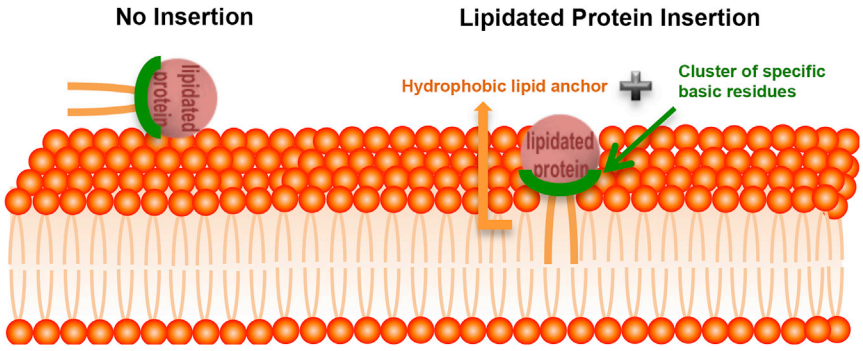

FIGURE 8 Schematic representation of the mechanism of lipidated-LC3 membrane insertion. The left part of the diagram shows an unproductive insertion event, with the protein's hydrophobic anchor not inserted into the membrane. Both the lipid anchor (control simulations) and key residues in the protein (experimental mutations) are necessary for insertion of the lipidated protein. These dynamic changes within the lipidated protein are induced by specific protein-lipid interactions. This specificity determines and facilitates PE insertion, as shown at the right of the diagram. To see this figure in color, go online.

process where the lipidated form of LC3 is involved in the assembly of the isolation membrane and further assists to form a vesicle, the autophagosome. To probe the membrane perturbations induced upon LC3 binding in our simulations, we calculated various parameters, including membrane thickness, density, and lateral pressure. During PE insertion, minor changes were observed in density and thickness, which equilibrate during the course of the simulation. However, an increase in the local spontaneous curvature upon LC3 insertion was found that is indicative of the curvature-inducing properties of LC3. Our results are consistent with a recent study on a lipid-anchored oligomer, which causes membrane perturbations by altering the lateral pressure (55). Our curvature results also highlight the underlying biological significance of the phagophore in autophagosome formation during autophagy. The lipidation process of LC3 family proteins is known to be sensitive to membrane curvature and lipid packing. A recent review on autophagic phagophore expansion suggests that additional anchor proteins involved during the initiation step (such as Atg3) add an additional level of spatial and temporal specificity to the lipid membrane insertion (57).

CONCLUSIONS

Macroautophagy is a conserved cellular recycling process essential for homeostasis and cell survival during stress. In response to stress, cellular components are sequestered into a growing phagophore that closes to form double membrane vesicles. The key to this process is the covalent conjugation of phosphatidylethanolamine (PE) to the LC3 protein that plays an important role in the formation of the autophagosome (28). The aim of this work was to reveal a reliable and robust mechanism of transition of cytoplasmic to membrane-inserted LC3-PE. This was accomplished by examining the events before, during, and after insertion of PE in silico. We have performed independent, unbiased CG MD simulations of LC3-PE, starting from aqueous-phase conformations placed far from the membrane. In this report, we explore lipidated LC3 dynamics with both zwitterionic phosphatidylcholine and a complex negatively charged bilayer composed of CL. Although prior experimental studies show that the PE attachment is required for the biological activity of the lipidated LC3 protein (28), dynamic characterization of the translocation of the cytoplasmic lipidated protein to the membrane-inserted form is challenging.

We propose that a basic patch of amino acid residues in α-helix III orients and steers the protein toward the membrane, acting as a specific determinant of membrane interaction. The final stage in reaching the membrane-inserted state involves hydrophobic forces of the lipid anchor to cross the membrane interface. Our data support the dual-recognition-mode hypothesis (56), with both protein and membrane lipids driving the permeation process (Fig. 8). In the scenario presented here, our findings thus provide a structural basis for the rational design of autophagic modulators targeting LC3 and possibly other lipidated proteins.

SUPPORTING MATERIAL

Five figures and two tables are available at http://www.biophysj.org/biophysj/supplemental/S0006-3495(15)00992-3.

AUTHOR CONTRIBUTIONS

L.T., D.S., and R.S.G. designed the study, analyzed the results, and drafted the manuscript. A.R. and D.M. perfomed live cell-based imaging experiments. N.A. performed heterogeneous bilayer simulations.

ACKNOWLEDGMENTS

We are indebted to CSIR-Fourth Paradigm Institute (4PI) for computational resources.

L.T. is funded by an INSPIRE Faculty Fellowship from the Department of Science and Technology. D.S. is funded by a Ramalingaswami Fellowship from the Department of Biotechnology. This work was supported by project BSC0302 to R.S.G. from the Council of Scientific and Industrial Research (CSIR) of India.

REFERENCES

1. Casey, P. J. 1995. Protein lipidation in cell signaling. *Science.* 268:221–225.
2. Hang, H. C., and M. E. Linder. 2011. Exploring protein lipidation with chemical biology. *Chem. Rev.* 111:6341–6358.

3. Wittinghofer, A., and I. R. Vetter. 2011. Structure-function relationships of the G domain, a canonical switch motif. *Annu. Rev. Biochem.* 80:943–971.
4. Thapar, R., J. G. Williams, and S. L. Campbell. 2004. NMR characterization of full-length farnesylated and non-farnesylated H-Ras and its implications for Raf activation. *J. Mol. Biol.* 343:1391–1408.
5. Kötting, C., J. Güldenhaupt, and K. Gerwert. 2012. Time-resolved FTIR spectroscopy for monitoring protein dynamics exemplified by functional studies of Ras protein bound to a lipid bilayer. *Chem. Phys.* 396:72–83.
6. Hannoush, R. N., and J. Sun. 2010. The chemical toolbox for monitoring protein fatty acylation and prenylation. *Nat. Chem. Biol.* 6:498–506.
7. Willumsen, B. M., A. Christensen, …, D. R. Lowy. 1984. The p21 *ras* C-terminus is required for transformation and membrane association. *Nature.* 310:583–586.
8. Hancock, J. F., A. I. Magee, …, C. J. Marshall. 1989. All *ras* proteins are polyisoprenylated but only some are palmitoylated. *Cell.* 57:1167–1177.
9. Vogel, A., C. P. Katzka, …, D. Huster. 2005. Lipid modifications of a Ras peptide exhibit altered packing and mobility versus host membrane as detected by ^{2}H solid-state NMR. *J. Am. Chem. Soc.* 127:12263–12272.
10. Brunsveld, L., J. Kuhlmann, …, H. Waldmann. 2006. Lipidated ras and rab peptides and proteins–synthesis, structure, and function. *Angew. Chem. Int. Ed. Engl.* 45:6622–6646.
11. Gorfe, A. A., R. Pellarin, and A. Caflisch. 2004. Membrane localization and flexibility of a lipidated ras peptide studied by molecular dynamics simulations. *J. Am. Chem. Soc.* 126:15277–15286.
12. Gorfe, A. A., M. Hanzal-Bayer, …, J. A. McCammon. 2007. Structure and dynamics of the full-length lipid-modified H-Ras protein in a 1,2-dimyristoylglycero-3-phosphocholine bilayer. *J. Med. Chem.* 50:674–684.
13. Gorfe, A. A., A. Babakhani, and J. A. McCammon. 2007. H-ras protein in a bilayer: interaction and structure perturbation. *J. Am. Chem. Soc.* 129:12280–12286.
14. Abankwa, D., A. A. Gorfe, …, J. F. Hancock. 2010. Ras membrane orientation and nanodomain localization generate isoform diversity. *Proc. Natl. Acad. Sci. USA.* 107:1130–1135.
15. Brunsveld, L., H. Waldmann, and D. Huster. 2009. Membrane binding of lipidated Ras peptides and proteins—the structural point of view. *Biochim. Biophys. Acta.* 1788:273–288.
16. Gorfe, A. A., A. Babakhani, and J. A. McCammon. 2007. Free energy profile of H-ras membrane anchor upon membrane insertion. *Angew. Chem. Int. Ed. Engl.* 46:8234–8237.
17. Huster, D., A. Vogel, …, K. Arnold. 2003. Membrane insertion of a lipidated ras peptide studied by FTIR, solid-state NMR, and neutron diffraction spectroscopy. *J. Am. Chem. Soc.* 125:4070–4079.
18. Reuther, G., K.-T. Tan, …, D. Huster. 2006. The lipidated membrane anchor of full length N-Ras protein shows an extensive dynamics as revealed by solid-state NMR spectroscopy. *J. Am. Chem. Soc.* 128:13840–13846.
19. Weise, K., S. Kapoor, …, R. Winter. 2011. Membrane-mediated induction and sorting of K-Ras microdomain signaling platforms. *J. Am. Chem. Soc.* 133:880–887.
20. Vogel, A., G. Reuther, …, D. Huster. 2010. Backbone conformational flexibility of the lipid modified membrane anchor of the human N-Ras protein investigated by solid-state NMR and molecular dynamics simulation. *Biochim. Biophys. Acta.* 1798:275–285.
21. Schroeder, H., R. Leventis, …, J. R. Silvius. 1997. S-Acylation and plasma membrane targeting of the farnesylated carboxyl-terminal peptide of N-ras in mammalian fibroblasts. *Biochemistry.* 36:13102–13109.
22. Sigal, C. T., W. Zhou, …, M. D. Resh. 1994. Amino-terminal basic residues of Src mediate membrane binding through electrostatic interaction with acidic phospholipids. *Proc. Natl. Acad. Sci. USA.* 91:12253–12257.
23. McLaughlin, S., and A. Aderem. 1995. The myristoyl-electrostatic switch: a modulator of reversible protein-membrane interactions. *Trends Biochem. Sci.* 20:272–276.
24. Gerlach, H., V. Laumann, …, M. Geyer. 2010. HIV-1 Nef membrane association depends on charge, curvature, composition and sequence. *Nat. Chem. Biol.* 6:46–53.
25. Sugawara, K., N. N. Suzuki, …, F. Inagaki. 2004. The crystal structure of microtubule-associated protein light chain 3, a mammalian homologue of *Saccharomyces cerevisiae* Atg8. *Genes Cells.* 9:611–618.
26. Ichimura, Y., T. Kirisako, …, Y. Ohsumi. 2000. A ubiquitin-like system mediates protein lipidation. *Nature.* 408:488–492.
27. Nakatogawa, H., Y. Ichimura, and Y. Ohsumi. 2007. Atg8, a ubiquitin-like protein required for autophagosome formation, mediates membrane tethering and hemifusion. *Cell.* 130:165–178.
28. Kabeya, Y., N. Mizushima, …, T. Yoshimori. 2000. LC3, a mammalian homologue of yeast Apg8p, is localized in autophagosome membranes after processing. *EMBO J.* 19:5720–5728.
29. Uemura, T., M. Yamamoto, …, S. Waguri. 2014. A cluster of thin tubular structures mediates transformation of the endoplasmic reticulum to autophagic isolation membrane. *Mol. Cell. Biol.* 34:1695–1706.
30. Schäfer, L. V., D. H. de Jong, …, S. J. Marrink. 2011. Lipid packing drives the segregation of transmembrane helices into disordered lipid domains in model membranes. *Proc. Natl. Acad. Sci. USA.* 108:1343–1348.
31. Sengupta, D., and A. Chattopadhyay. 2012. Identification of cholesterol binding sites in the serotonin1A receptor. *J. Phys. Chem. B.* 116:12991–12996.
32. Arnarez, C., J.-P. Mazat, …, X. Periole. 2013. Evidence for cardiolipin binding sites on the membrane-exposed surface of the cytochrome *bc*1. *J. Am. Chem. Soc.* 135:3112–3120.
33. Marrink, S. J., and D. P. Tieleman. 2013. Perspective on the Martini model. *Chem. Soc. Rev.* 42:6801–6822.
34. Kirisako, T., Y. Ichimura, …, Y. Ohsumi. 2000. The reversible modification regulates the membrane-binding state of Apg8/Aut7 essential for autophagy and the cytoplasm to vacuole targeting pathway. *J. Cell Biol.* 151:263–276.
35. Marrink, S. J., H. J. Risselada, …, A. H. de Vries. 2007. The MARTINI force field: coarse grained model for biomolecular simulations. *J. Phys. Chem. B.* 111:7812–7824.
36. Monticelli, L., S. K. Kandasamy, …, S.-J. Marrink. 2008. The MARTINI coarse-grained force field: extension to proteins. *J. Mol. Model.* 4:819–834.
37. de Jong, D. H., X. Periole, and S. J. Marrink. 2012. Dimerization of amino acid side chains: lessons from the comparison of different force fields. *J. Chem. Theory Comput.* 8:1003–1014.
38. Chu, C. T., J. Ji, …, V. E. Kagan. 2013. Cardiolipin externalization to the outer mitochondrial membrane acts as an elimination signal for mitophagy in neuronal cells. *Nat. Cell Biol.* 15:1197–1205.
39. Karo, J., P. Peterson, and M. Vendelin. 2012. Molecular dynamics simulations of creatine kinase and adenine nucleotide translocase in mitochondrial membrane patch. *J. Biol. Chem.* 287:7467–7476.
40. Pronk, S., S. Páll, …, E. Lindahl. 2013. GROMACS 4.5: a high-throughput and highly parallel open source molecular simulation toolkit. *Bioinformatics.* 29:845–854.
41. Berendsen, H. J., J. P. M. Postma, …, J. Haak. 1984. Molecular dynamics with coupling to an external bath. *J. Chem. Phys.* 81:3684–3690.
42. Castillo, N., L. Monticelli, …, D. P. Tieleman. 2013. Free energy of WALP23 dimer association in DMPC, DPPC, and DOPC bilayers. *Chem. Phys. Lipids.* 169:95–105.
43. Ollila, O. H., H. J. Risselada, …, S. J. Marrink. 2009. 3D pressure field in lipid membranes and membrane-protein complexes. *Phys. Rev. Lett.* 102:078101.

44. Sengupta, D. 2012. Cholesterol modulates the structure, binding modes, and energetics of caveolin-membrane interactions. *J. Phys. Chem. B.* 116:14556–14564.

45. Patil, K. M., R. J. Naik, …, V. A. Kumar. 2012. Highly efficient (R-X-R)-type carbamates as molecular transporters for cellular delivery. *J. Am. Chem. Soc.* 134:7196–7199.

46. Liu, C., H. Ma, …, L. Yu. 2013. Arginine68 is an essential residue for the C-terminal cleavage of human Atg8 family proteins. *BMC Cell Biol.* 14:27.

47. Zimmerberg, J., and M. M. Kozlov. 2006. How proteins produce cellular membrane curvature. *Nat. Rev. Mol. Cell Biol.* 7:9–19.

48. Helfrich, W. 1981. Amphiphilic mesophases made of defects. *In* Physique des défauts (Physics of defects). R. Balian, M. Kleman, and J.-P. Poirier, editors. North-Holland, Amsterdam, pp. 716–755.

49. Deserno, M. 2015. Fluid lipid membranes: from differential geometry to curvature stresses. *Chem. Phys. Lipids.* 185:11–45.

50. Marrink, S. J., A. H. de Vries, and D. P. Tieleman. 2009. Lipids on the move: simulations of membrane pores, domains, stalks and curves. *Biochim. Biophys. Acta.* 1788:149–168.

51. Hu, Y., S. Ou, and S. Patel. 2013. Free energetics of arginine permeation into model DMPC lipid bilayers: coupling of effective counterion concentration and lateral bilayer dimensions. *J. Phys. Chem. B.* 117:11641–11653.

52. Ahearn, I. M., K. Haigis, …, M. R. Philips. 2012. Regulating the regulator: post-translational modification of RAS. *Nat. Rev. Mol. Cell Biol.* 13:39–51.

53. Jensen, M. Ø., O. G. Mouritsen, and G. H. Peters. 2004. Simulations of a membrane-anchored peptide: structure, dynamics, and influence on bilayer properties. *Biophys. J.* 86:3556–3575.

54. Vogel, A., K.-T. Tan, …, D. Huster. 2007. Flexibility of ras lipid modifications studied by ^{2}H solid-state NMR and molecular dynamics simulations. *Biophys. J.* 93:2697–2712.

55. Li, H., and A. A. Gorfe. 2014. Membrane remodeling by surface-bound protein aggregates: insights from coarse-grained molecular dynamics simulation. *J. Phys. Chem. Lett.* 5:1457–1462.

56. Lumb, C. N., J. He, …, M. S. Sansom. 2011. Biophysical and computational studies of membrane penetration by the GRP1 pleckstrin homology domain. *Structure.* 19:1338–1346.

57. Johansen, T., and T. Lamark. 2014. Selective autophagy goes exclusive. *Nat. Cell Biol.* 16:395–397.